RESEARCH ARTICLE

From Agri-Waste to High-Performance Material: Synthesis of Rice Husk Activated Carbon (RAC) and Rice Husk Activated Carbon / Copper Oxide (RACU) for Electrochemical Performance

Jinitha C.G[1], Abisha.P[2] and Sonia S[3]*

[1]Research Scholar (Reg. No. 19213042132016), Department of Physics, Holy Cross College (Autonomous), Nagercoil, Kanyakumari District (Affiliated to Manonmaniam Sundaranar University, Abishekapatti, Tirunelveli) Tamil Nadu, India.
[2]Research Scholar (Reg. No. 20213042132005), Department of Physics, Holy Cross College (Autonomous), Nagercoil, Kanyakumari District (Affiliated to Manonmaniam Sundaranar University, Abishekapatti, Tirunelveli) Tamil Nadu, India.
[3]Assistant Professor, Department of Physics, Holy Cross College (Autonomous), Nagercoil-629004, Kanyakumari District (Affiliated to Manonmaniam Sundaranar University, Abishekapatti, Tirunelveli) Tamil Nadu, India.

*Address for Correspondence
Sonia S[3]*
Assistant Professor,
Department of Physics,
Holy Cross College (Autonomous),
Nagercoil-629004, Kanyakumari District
(Affiliated to Manonmaniam Sundaranar University, Abishekapatti, Tirunelveli)
Tamil Nadu, India.
Email: sonianst10@gmail.com

ABSTRACT

Biomass-derived activated carbon is an economically viable and environmentally friendly option for electrochemical applications due to its low cost, renewable nature, and extensive availability. The primary objective of this study is to develop a method for extracting activated carbon from rice husk through the use of a carbonization procedure. Analyses conducted with scanning electron microscopy (SEM) produced precise renderings of the structure's unique characteristics. In addition, an X-ray Diffraction (XRD) study was performed, and the results confirmed the existence of graphitic peaks, as well as copper oxide. Cyclic voltammetry (also known as CV) was utilized to carry out electrochemical analysis at a scan rate that varied from five to one hundred. Notably, the scan rate of 10 m V/s corresponded to the point where the maximum capacitance was measured, which was 167.36 F g^{-1}. The power density that was attained was 2083 W kg^{-1}, and the energy density was also 5.2 Wh kg^{-1}. The level

of resistance was calculated to be 0.63Ω. These results strongly suggest that the synthesized material is suitable for future research and electrochemical applications.

Keywords: Biomass, Activated Carbon, Rice Husk, Electrochemical Applications, Carbonization.

INTRODUCTION

Climate change and the depletion of non-renewable energy sources have accelerated the development of renewable energy sources and demanded the development of efficient energy storage solutions[1–7]. Given the rapid growth of society and the increasing emphasis placed on green energy solutions, there has been significant interest and attention directed toward energy storage devices[8].Electrochemistry plays a crucial role in energy storage devices, as it governs the fundamental processes that enable these devices to store and release energy efficiently[9].Electrochemical applications span a broad spectrum of areas, encompassing electrode materials[10,11] and batteries[12], electrocatalysis[13], electroanalysis, and electrochemical sensors[14], as well as the broad areas of energy and fuel[15]. Activated carbon and its composites have significant promise in the realm of electrochemistry due to their distinctive characteristics[16].

Biomass has attracted considerable attention in the domain of renewable energy sources due to its ample availability and its recognition as an environmentally friendly, sustainable, and ecologically sound resource[17].Carbon and electrodes made with carbon are widely employed in various energy storage systems due to their low cost, their resistance to heat, their ability to be processed, and their adaptability in terms of their structure and texture to match the requirements of specific applications. The addition of hierarchically porous structures further improves the material's specific surface area, enabling fast ion transportation[18–20]. This research work uses rice husk activated carbon and copper oxide as the electrode material due to its unique properties. Copper (II) oxide (CuO) is classified as a type-p semiconductor material with a small band gap energy of 1.2 eV and good catalytic, optical, electrical, magnetic, and biological capabilities among nanostructured oxides[21]. Due to these fascinating properties, CuO nanostructures have been reported to have a wide range of practical applications, includingmagnetic storage,catalysis, gas sensor, solar cell, lithium battery, biosensor, and antifungal/antimicrobial agents in the agriculture and health sectors, photocatalysts for wastewater treatment, etc[22]. According to the findings of this paper, copper oxide (CuO) infused with activated carbon has been performing very well as a candidate for use as an electrode material.

The study focuses on the preparation of activated carbon from rice husk biomass (RAC), synthesizing copper oxide using hydrothermal methods, and creating composite materials using ultrasonication, followed by an analysis and comparison of its electrochemical characteristics.The physical and chemical characteristics of biomass were studied using X-ray diffractometry (XRD), Raman spectroscopy, and Fourier transform infrared (FTIR) spectrophotometry. The analysis of the chemical properties of biomass was conducted by elemental analysis. Furthermore, high-resolution scanning electron microscopy (SEM), cyclic voltammetry (CV), galvanostatic charge-discharge (GCD), and electrochemical impedance spectroscopy (EIS) techniques were employed to examine the structural and electrochemical properties of activated carbon.

MATERIALS AND METHODS

Rice husks were sourced from agricultural regions. All chemicals, including sulfuric acid (H_2SO_4), copper sulfate ($CuSO_4$), sodium hydroxide (NaOH), and ethanol met the exacting standards for Analytical Reagent (AR) grade quality. Furthermore, to maintain the highest level of purity, double-distilled water was exclusively used throughout the entire experiment.

Jinitha *et al.,*

Synthesis of RAC/CuO nanocomposites
Rice husks are the biomass material used to synthesise activated carbon. The rice husks used in this investigation were obtained from the agricultural areas located in Kanyakumari, Tamil Nadu, India. The synthesis process of RACU sample is shown in fig 1, in which the rice husks were subjected to a rigorous preparation procedure, commencing with a comprehensive cleansing with double distilled water. Subsequently, rice husk material was allowed to undergo natural drying for a duration of three days. Subsequently, the husks were submerged in sulfuric acid for a duration of 24 hours, leading to the formation of a viscous and black mixture. The slurry was afterwards filtered and then underwent carbonization at a temperature of 400°C for a duration of two hours. The resulting black powder was meticulously pulverised to achieve consistent particle size, hence functioning as the activated carbon for the production of electrode material. The activated carbon sample is designated as "RAC" for the purpose of sample identification.

Copper oxide was created in a lab setting by combining 0.2M $CuSO_4$ and 0.5M NaOH in a 1:1 ratio. The NaOH solution was added to the $CuSO_4$ solution drop by drop, producing a precipitate with a grey colour. The resultant precipitate is then put into a Teflon-coated autoclave and heated to a temperature of 160°C for 12 hours to produce CuO.An ultrasonicator is used to synthesize the composite material using Rice Husk Activated Carbon (RAC) and Copper Oxide (CuO). The process involves a controlled laboratory environment, where high-frequency sound waves generate vibrations and cavitation effects, resulting in a homogeneous composite with uniform CuO particle distribution. The process is monitored for optimal mixing and dispersion, offering potential benefits in various fields. The nanocomposite of RAC/CuO is labelled as RACU.

Characterization
A PAN analytical (XPERT-PRO) X-ray diffractometer using Cu Ka1 radiation (k = 1.5406 Å) was employed to characterize the crystallographic properties of the samples. The surface morphologies were characterized by a FEI Quanta-250 Field Emission Scanning Electron Microscopy (FESEM) coupled with EDX. FT-IR analysis was performed by Bruker Tensor 27, Fourier Transforms Infrared spectroscope. The specific surface areas and pore sizes were determined from BET-N_2adsorption-desorption isotherms using a micromeritics ASAP 2020 surface area analyzer. Electrochemical impedance spectroscopy (EIS) and cyclic voltammetry (CV) were utilised on a Biologic VMP-300 electrochemical working station for the purpose of determining the electrochemical behaviour of RAC/CuO-based working electrodes.

RESULTS AND DISCUSSION

X-Ray Diffraction (XRD) analysis
The X-ray diffraction (XRD) patterns presented in Figure 2 (a) elucidate the diffraction profiles of both Copper Oxide (CuO) and the RAC/CuO composites at varying ratios (1:1, 1:2, and 1:3), labeled as RACU1, RACU2, and RACU3 respectively. Clear peaks were observed at specific 2θ angles, notably 32.41° (110), 35.39° (002), 38.59° (111), and others, corresponding to distinct facets of the monoclinic phase of CuO within the C2/c Space Group. These findings closely align with the JCPDS Reference code: 00-041-0254. The lattice parameters were determined as a (Å): 4.6850, b (Å): 3.4230, and c (Å): 5.1320. The calculated density was 6.51 g/cm3, while the empirical density registered slightly lower at 6.45 g/cm^3, with a cell volume of 81.17 x 106 pm3. The Scherrer formula is employed to derive the average grain size of the samples[23].

$$D = 0.89\, \lambda\, /\, \beta\, \cos\theta \qquad (1)$$

The prominent peaks at 2θ = 35.39° and 38.59° definitively affirm the presence of the pure monoclinic phase of CuO. Moreover, the average grain size of copper oxide, as determined by the Scherrer formula, fell within an estimated range of 42-61 nm.Table 1, shows the Average crystalline size, dislocation density and strain of the CuO and RACU samples.

Jinitha *et al.,*

In Figure 2 (b), the XRD patterns of the Rice Husk Activated Carbon (RAC) material are presented. The wide diffraction peak at (002) with 2θ ranging from 15-35º is indicative of amorphous carbon structures. Additionally, the faint and broad (101) diffraction peak at 2θ = 40-50º arises from the *a*-axis of the graphite structure[24–30].

Field Emission Scanning Electron Microscopy (FESEM) analysis

The morphological characteristics of the synthesized CuO nanostructures and the composite RAC/CuO samples (referred to as RACU1, RACU2, and RACU3) were comprehensively examined using Field Emission Scanning Electron Microscopy (FESEM), as illustrated in Figure 3. This analysis offers critical insights into the structural features and particle arrangement, laying the foundation for a detailed understanding of their properties and potential applications. Fig 3(a and b) shows the SEM image of CuO nanostructures has a layered structure that is composed of numerous nanoplatelets, with an average particle width of 27.30 nm. In Figure 3(c and d), the SEM depiction of RAC/CuO nanoparticles at a 1:1 ratio (designated as RACU1) unveils a structured assembly of various nanoplatelets, forming a layered architecture. These nanoplatelets possess an average width of 23.80 nm. Figure 3 (e and f) displays the scanning electron microscopy (SEM) image of RAC/CuO nanoparticles in a ratio of 1:2 (RACU2). The image reveals the presence of nanostructures characterized by a layered arrangement consisting of several nanoplatelets. The average width of these particles is measured to be 28.16 nm. Figure 3(g and h) depicts the scanning electron microscopy (SEM) image of RAC/CuO nanoparticles in a ratio of 1:3 (RACU3). The image reveals the presence of nanostructures exhibiting a layered configuration, consisting of a multitude of nanoplatelets. The average width of these particles is measured to be 21.82 nm.The utilization of a layered nanostructure including numerous thin leaves holds significant potential for enhancing the performance of as-derived samples. This is primarily attributed to the substantial specific surface area resulting from the intricate fine structure, which in turn provides a greater number of active surface absorption sites[31]. Fig 3(i-l) shows the particle distribution curves of the samples CuO, RACU1, RACU2 and RACU3 respectively.

Energy Dispersive X-ray Spectroscopy (EDX)analysis

The EDX examination revealed the components that were present in the RAC, CuO, RACU1, RACU2, and RACU3 sample, and they are presented in Figure 4(a-e). Figure 4(a) substantiates the presence of carbon within the RAC (Rice Husk Activated Carbon) sample. Figure 4(b) provides evidence confirming the presence of both copper and oxygen within the CuO (Copper Oxide) sample. Figures 4(c-e) distinctly depict the existence of carbon, copper, and oxygen in the RACU1, RACU2, and RACU3 samples, respectively. Furthermore, Figure 4(e) highlights a minute quantity of cobalt, possibly stemming from instrumental or handling discrepancies.

Fourier-Transform Infrared Spectroscopy (FTIR) analysis

The FTIR spectrum, illustrated in Figure 5, encompasses the synthesized RAC, CuO, as well as RACU1, RACU2, and RACU3 nanoparticles. In the case of copper oxide nanoparticles, the peaks at approximately 680, 607, and 504 cm^{-1} pertain to the Cu–O stretching vibrations characteristic of the monoclinic structure. The absorption bands at 3428 cm^{-1} and 1621 cm^{-1} are attributed to the OH stretching vibrations and HOH bending mode of adsorbed water molecules. This occurrence is linked to the high surface area to volume ratio of nanocrystalline materials, facilitating moisture absorption within the lattice. Additionally, the absorption band at 1114 cm^{-1} aligns with the C–O stretching of phenolic and alcoholic compounds.

For the RAC and RACU samples, the spectral region around 3600 cm^{-1} indicates O-H stretching vibrations, signifying the presence of hydroxyl groups. Bands at 3515 cm^{-1} may also relate to O-H stretching or other hydrogen-bonding functional groups. The bands at 2921 cm^{-1} suggest vibrational modes linked to C-H stretching, indicating aliphatic or aromatic hydrocarbon groups. The bands at 2848 cm^{-1} strongly imply C-H stretching, commonly associated with aliphatic hydrocarbons or methyl groups. At 2373 cm^{-1}, a distinct functional group might exist, yet its exact nature remains uncertain. Around 2305 cm^{-1}, further context is needed for accurate interpretation. Peaks at 1748 cm^{-1} denote C=O stretching, indicating carbonyl groups present in compounds like ketones, aldehydes, and carboxylic acids. Around 1530 cm^{-1}, the presence of aromatic compounds is indicated by C=C stretching. At 1374 cm^{-1}, C-H bending,

often seen in aromatic compounds, may be present. The bands at 1023 cm^{-1} reveal C-O stretching, suggesting the existence of various oxygen-containing functional groups like ethers, alcohols, and phenols.

Raman Spectroscopy

Raman spectroscopy is a method employed for assessing the molecular vibrations and rotational energies of samples, allowing for substance identification and material analysis. Moreover, it serves as a valuable tool in characterizing the structural attributes of carbon-based materials. As depicted in Figure 6, the Raman spectra of RAC, RACU1, RACU2, and RACU3 are presented. Among these, the spectra of RAC and RACU3 distinctly exhibit the characteristic D and G bands, positioned around 1375 cm^{-1} (D band) and 1590 cm^{-1} (G band), which are hallmark features in carbon material spectra. Notably, only RAC and RACU3 demonstrate D and G peaks across the entire spectral range, whereas in RACU2 and RACU1, these peaks are less prominent due to the reduced ratio of carbon material. Nevertheless, in RACU2 and RACU1, two peaks emerge at approximately 287 cm^{-1} and 616 cm^{-1}, attributable to the (1:2) and (1:1) ratios of RAC/CuO which are the RACU2 and RACU1 samples, respectively. The Raman spectra of hydrothermally produced RACU2 and RACU1, with visible peaks due to the A_g and B_g modes of CuO exhibiting notable shifts towards lower wavenumbers, accompanied by a broadening effect. Specifically, for RACU2 and RACU1, the values of A_g and B_g modes are 287 cm^{-1}, and 616 cm^{-1} signifying a clear influence of the hydrothermal growth process on the nanomaterial properties of CuO. These wavenumbers are comparable to those cited in the scientific literature[32,33].

Electrochemical analysis
Brunauer-Emmett-Teller (BET) & Barrett-Joyner-Halenda (BJH)
The N$_2$ adsorption-desorption isotherms were employed to assess the porous architecture and pore size distribution of both the Rice Husk Activated Carbon (RAC) and RACU3 materials. The BET analysis of these materials is presented in Figure 7. Illustrated in Figures 7 (b) and 7 (e), the isotherms of RAC and RACU3 respectively, which displays the characteristic Type IV behavior, accompanied by an observable hysteresis slope at elevated relative pressures, signifying the presence of both mesoporosity and macroporosity [33]. For RACU3, the specific surface area was determined as 21.58 m^2 g^{-1}, with a micropore volume of 0.1008 cm^3 g^{-1}. In contrast, RAC exhibited a specific surface area of 21.30 m^2 g^{-1}, along with a micropore volume of 0.0564 cm^3 g^{-1}. In terms of their surface areas, it's notable that RACU3 possesses a greater surface area compared to that of RAC. The parameter of fitting line, BET constant and specific surface area are given in Table 2.

The BET analysis was conducted to investigate the properties of both RAC and RACU3 nanocomposites. The methodology employed in the BET measurement, as illustrated in Figure 7 (c and f), involves plotting *PV (P$_0$ − P)* against relative pressures *P/P$_0$*. This graphical representation enables the calculation of essential parameters such as Slope (s), Intercept (i), and BET constant (C), thereby facilitating the determination of the specific surface area. Notably, the computed specific surface area for RAC is measured at 21.3 m^2/g, while for RO3, a significant increase is observed, reaching 21.58 m^2/g. The higher micropore volume in RACU3, which measures at 0.1003 cm^{3}g^{-1} compared to RAC with a volume of 0.0564 cm^{3}g^{-1}, signifies that RACU3 possesses a larger proportion of micropores. This suggests that RACU3 possesses a greater capacity for ion storage within its micropores. As a result, RACU3 may exhibit enhanced charge storage capabilities and improved electrochemical performance compared to RAC. This can be particularly beneficial in applications where high capacity and efficient charge-discharge cycling are critical factors.

Upon analysing the pore size distributions illustrated in Figures 7 (a and d) for RAC and RACU3 respectively and, the average pore diameter for RAC is 10.6nm and for RACU3 it is 18nm. The larger average pore diameter of RACU3 (18nm) compared to RAC (10.6nm) indicates a more substantial mesoporous structure. This suggests that RACU3 can potentially accommodate larger ions and molecules within its pores, enhancing ion diffusion kinetics during charge and discharge processes. Consequently, RACU3 may exhibit improved electrolyte accessibility and ion transport, contributing to enhanced electrochemical performance, especially in applications requiring rapid and efficient charge transfer.

Jinitha *et al.,*

Cyclic Voltammetry

The cyclic voltammetry (CV) profiles of the RAC and RACU3 samples, presented in Figure 8 (a and b), involved various scan rates while maintaining a consistent potential range of 0.0 to 1.0 V. In Figure 8 (a and b), it is evident that the RAC sample exhibits a symmetrical behavior, even at higher scan rates. This underscores its notable capacitive properties and swift charge-discharge mechanisms, which can be attributed to effective electrolyte permeation to the electroactive surface. Conversely, the absence of discernible redox or oxidation peaks in the CV curve of the RACU3 material indicates limited electron transfer processes, suggesting lower electroactivity under the experimental conditions. This implies a potential lack of active electrochemical sites or necessary chemical species for significant electron transfer. The low area under the CV curve further supports this, indicating a relatively modest charge storage capacity. This insight is crucial for understanding the electrochemical behavior and potential applications of the rice husk activated carbon/Copper oxide material. Further exploration may be necessary to enhance its electroactivity or investigate alternative applications for this composite material.

Figure 8(c) presents the specific capacitance values of the RAC and RACU3 samples at different scan rates. Notably, the assessment of specific capacitance at a scan rate of 10 mV/s yielded values of 594.89 F g^{-1} for RAC and 167.36 F g^{-1} for RACU3. As expected, the RAC sample displayed distinct pairs of peaks originating from faradaic redox reactions, indicative of its characteristic pseudo-capacitive traits. Conversely, the RACU3 sample exhibited a notably smaller integrated area under the CV curve, affirming its lower specific capacitance of 167.36 F g^{-1}.

Electrochemical Impedance

The Nyquist plots in Figure 9 (a and b) provide a detailed view of the electrical behavior of both RAC (rice husk activated carbon) and RACU3 (Rice husk activated carbon/ copper oxide in 1:3 ratio) across a wide frequency range from 100 kHz to 0.01 Hz, under a 5 mV perturbation. In the high-frequency region, the point where the semicircle intersects with the real axis represents the Equivalent Series Resistance (ESR). This parameter encompasses factors like the resistance of the electrolyte solution, the intrinsic resistance of the active material, and the contact resistance at the interface between the active material and the current collector. The intersection on the abscissa of the Nyquist plots specifically indicates the ESR within the three-electrode system. The calculated charge transport resistances are 2.45Ω for RAC and 0.63Ω for RACU3. These values highlight the electrodes' ability to maintain low resistance while facilitating a favourable ion response. Upon close examination, a clear trend of reduced resistance is observed for both RAC and RACU3 samples, with RAC exhibiting a relatively higher resistance of 2.45Ω compared to RACU3's 0.63Ω. This disparity indicates that the RACU3 specimen possesses a lower resistance profile compared to its RAC counterpart.

The reduction in resistance values observed in the RACU3 specimen compared to RAC can be attributed to the incorporation of copper oxide (CuO) in the composite material. Copper oxide is known to enhance electrical conductivity due to its semiconducting properties. This means it facilitates the movement of electrons within the material, reducing overall resistance. Additionally, the structure and morphology of the composite material may have contributed to this effect, allowing for improved charge transport. Overall, the presence of copper oxide in the composite material leads to a more conductive and less resistive system.

Galvanostatic Charge-Discharge (GCD)

The galvanostatic charging-discharging (GCD) analysis, as depicted in Figure 10 (a and b), provides an insightful view into the electrochemical behavior of both rice husk activated carbon (RAC) and RACU3 (Rice husk activated carbon/ copper oxide in a 1:3 ratio). This investigation was conducted across a consistent potential range of 0 to 1 V, employing diverse current densities ranging from 0.5 to 20 mA. The notable symmetry observed in the charge/discharge curves indicates exceptional coulombic efficiency. The profiles displayed in Figure 10 showcase the electrochemical performance of RAC and RACU3, at varying current densities. The symmetric triangular morphology of the curves suggests favourable electrochemical behavior. It's worth noting that the voltage-time responses exhibit some deviation from a purely linear correlation, likely attributed to the involvement of pseudocapacitance effects arising from Faradaic reactions [34].

Ragone Plot

A Ragone plot provides a visual means to compare the performance of different energy storage technologies, like batteries, capacitors, or fuel cells, by evaluating their energy density (Wh/kg) and power density (W/kg). Each point on this plot represents a specific energy storage technology, and its position shows the balance between energy storage capacity and the speed of energy discharge. Striking the right balance is crucial depending on specific application requirements, often requiring a trade-off between high energy density for longer-lasting energy supply and high-power density for rapid energy delivery. In Figure 11 (a and b), the Ragone plots of RAC reveal an intriguing trend. Here, an increase in power density, from 2272 to 4545 W kg^{-1}, is coupled with a decrease in energy density, from 4.4 to 2.5 Wh kg^{-1}. Similarly, for RACU3, an increase in power density, from 2083 to 5000 W kg^{-1}, leads to a reduction in energy density, from 5.2 to 0.5 Wh kg^{-1}. This trend underscores the trade-off between high power output and energy storage capacity.

It's noteworthy that even at a power density of 2083 W kg^{-1}, the energy density of RACU3 composites remains notably high at 5.2 Wh kg^{-1}. This highlights the composite's ability to maintain a commendable energy storage capacity over a substantial power range, which is a favourable characteristic for certain applications. This versatility could make it an excellent candidate for various energy storage applications, where both high-power output and substantial energy storage capacity are required.

CONCLUSION

This research addresses the urgent need for efficient energy storage solutions in light of climate change and dwindling non-renewable energy sources. It focuses on utilizing rice husk activated carbon (RAC) and copper oxide for electrode materials, leveraging their unique properties. Copper oxide (CuO) exhibits remarkable semiconductor characteristics and versatile practical applications. The study's thorough characterization involves techniques such as XRD, Raman spectroscopy, FTIR, and SEM to analyze the physical and chemical properties of the materials. The electrochemical analysis results highlight the significant potential of CuO-decorated RAC composites in advancing energy storage technologies, showcasing promise for a sustainable energy future. In summary, the comprehensive characterization analysis yielded crucial numerical values for the CuO-decorated rice husk activated carbon (RAC/CuO) composites. This included lattice parameters of a = 4.6850 Å, b = 3.4230 Å, and c = 5.1320 Å for CuO, along with an average grain size range of 42-61 nm. Field Emission Scanning Electron Microscopy (FESEM) provided key measurements, indicating average particle widths ranging from 21.82 to 28.16 nm. Energy Dispersive X-ray Spectroscopy (EDX) confirmed the elemental composition of carbon, copper, and oxygen in the samples. Fourier-Transform Infrared Spectroscopy (FTIR) highlighted distinctive peaks associated with various functional groups. Raman spectroscopy revealed characteristic bands, while specific capacitance values from Cyclic Voltammetry (CV) showed RAC with 594.89 F g^{-1} and RACU3 with 167.36 F g^{-1} at a scan rate of 10 mV/s. Electrochemical Impedance analysis demonstrated lower resistances, with charge transport resistances of 2.45Ω for RAC and 0.63Ω for RACU3. Galvanostatic Charge-Discharge (GCD) analysis illustrated coulombic efficiency, and Ragone plots depicted a trade-off between power and energy density. Remarkably, even at a power density of 2083 W kg^{-1}, RACU3 maintained a high energy density of 5.2 Wh kg^{-1}, showcasing its suitability for applications necessitating a balanced combination of high-power output and substantial energy storage capacity. This versatility positions the RAC/CuO composites as promising candidates for a wide array of energy storage applications.

REFERENCES

1. Lu X, Yu M, Wang G, Tong Y, Li Y. Flexible solid-state supercapacitors: design, fabrication and applications. Energy Environ Sci 2014; 7:2160–2181.
2. Yi H, Nakabayashi K, Yoon S-H, Miyawaki J. Study on the applicability of pressurized physically activated carbon as an adsorbent in adsorption heat pumps. RSC Advances 2022;12:2558–2563.

3. Ding Y, Qi J, Hou R, Liu B, Yao S, Lang J, Chen J, Yang B. Preparation of High-Performance Hierarchical Porous Activated Carbon via a Multistep Physical Activation Method for Supercapacitors. Energy Fuels 2022; 36:5456–5464.

4. Lin B, Wang Y. Inconsistency of economic growth and electricity consumption in China: A panel VAR approach. Journal of Cleaner Production 2019; 229:144–156.

5. Majumdar A. A new industrial revolution for a sustainable energy future. MRS Bulletin 2013; 38:947–954.

6. Rolison DR, Nazar LF. Electrochemical energy storage to power the 21st century. MRS Bulletin 2011; 36:486–493.

7. Guo Y, Wang K, Hong Y, Wu H, Zhang Q. Recent progress on pristine two-dimensional metal–organic frameworks as active components in supercapacitors. Dalton Trans 2021; 50:11331–11346.

8. Yang J, Liu Y, Liu S, Li L, Zhang C, Liu T. Conducting polymer composites: material synthesis and applications in electrochemical capacitive energy storage. Materials Chemistry Frontiers 2017; 1:251–268.

9. Kebede AA, Kalogiannis T, Van Mierlo J, Berecibar M. A comprehensive review of stationary energy storage devices for large scale renewable energy sources grid integration. Renewable and Sustainable Energy Reviews 2022; 159:112213.

10. Boamah R, Agyei-Tuffour B, Dodoo-Arhin D, Nyankson E, Brobbey KJ, Obada D, Mohammed L. Activated cashew carbon-manganese oxide based electrodes for supercapacitor applications. Scientific African 2023; 20:e01647.

11. Wang W, Cao J, Yu J, Tian F, Luo X, Hao Y, Huang J, Wang F, Zhou W, Xu J, Liu X, Yang H. Flexible Supercapacitors Based on Stretchable Conducting Polymer Electrodes. Polymers 2023; 15:1856.

12. Yu X, Manthiram A. Sustainable Battery Materials for Next-Generation Electrical Energy Storage. Advanced Energy and Sustainability Research 2021; 2:2000102.

13. Bi H, Wang K, Xu C, Wang M, Chen B, Fang Y, Tan X, Zeng J, Tan T. Biofuel synthesis from carbon dioxide via a bio-electrocatalysis system. Chem Catalysis 2023; 3:100557.

14. Silva LRG, Carvalho JHS, Stefano JS, Oliveira GG, Prakash J, Janegitz BC. Electrochemical sensors and biosensors based on nanodiamonds: A review. Materials Today Communications 2023; 35:106142.

15. Yan B. Chapter 1 - Metal-organic frameworks (MOFs), rare earth MOFs, and rare earth functionalized MOF hybrid materials. In: Yan B, editor. Rare Earth Metal-Organic Framework Hybrid Materials for Luminescence Responsive Chemical Sensors. Woodhead Publishing; 2022. p. 3–40.

16. Ndagijimana P, Rong H, Ndokoye P, Mwizerwa JP, Nkinahamira F, Luo S, Guo D, Cui B. A review on activated carbon/ graphene composite-based materials: Synthesis and applications. Journal of Cleaner Production 2023; 417:138006.

17. Saleem M. Possibility of utilizing agriculture biomass as a renewable and sustainable future energy source. Heliyon 2022; 8:e08905.

18. Borchardt L, Leistenschneider D, Haase J, Dvoyashkin M. Revising the Concept of Pore Hierarchy for Ionic Transport in Carbon Materials for Supercapacitors. Advanced Energy Materials 2018; 8:1800892.

19. Xu Y, Lin Z, Zhong X, Huang X, Weiss NO, Huang Y, Duan X. Holey graphene frameworks for highly efficient capacitive energy storage. Nat Commun 2014; 5:4554.

20. Liu T, Zhang F, Song Y, Li Y. Revitalizing carbon supercapacitor electrodes with hierarchical porous structures. J Mater Chem A 2017; 5:17705–17733.

21. Bopape DA, Mathobela S, Matinise N, Motaung DE, Hintsho-Mbita NC. Green Synthesis of CuO-TiO2 Nanoparticles for the Degradation of Organic Pollutants: Physical, Optical and Electrochemical Properties. Catalysts 2023; 13:163.

22. Phang Y-K, Aminuzzaman M, Akhtaruzzaman M, Muhammad G, Ogawa S, Watanabe A, Tey L-H. Green Synthesis and Characterization of CuO Nanoparticles Derived from Papaya Peel Extract for the Photocatalytic Degradation of Palm Oil Mill Effluent (POME). Sustainability 2021; 13:796.

23. Bouazizi N, Bargougui R, Oueslati A, Benslama R. Effect Of Synthesis Time On Structural, Optical And Electrical Properties Of CuO Nanoparticles Synthesized By Reflux Condensation Method. ADVANCED MATERIALS Letters 2014; 2015:158–164.

24. Hara M, Yoshida T, Takagaki A, Takata T, Kondo JN, Hayashi S, Domen K. A carbon material as a strong protonic acid. Angew Chem Int Ed Engl 2004; 43:2955–2958.

25. Toda M, Takagaki A, Okamura M, Kondo JN, Hayashi S, Domen K, Hara M. Biodiesel made with sugar catalyst. Nature 2005; 438:178–178.

26. Okamura M, Takagaki A, Toda M, Kondo JN, Domen K, Tatsumi T, Hara M, Hayashi S. Acid-Catalyzed Reactions on Flexible Polycyclic Aromatic Carbon in Amorphous Carbon. Chem Mater 2006; 18:3039–3045.

27. Takagaki A, Toda M, Okamura M, Kondo JN, Hayashi S, Domen K, Hara M. Esterification of higher fatty acids by a novel strong solid acid. Catalysis Today 2006; 116:157–161.

28. Suganuma S, Nakajima K, Kitano M, Yamaguchi D, Kato H, Hayashi S, Hara M. Hydrolysis of Cellulose by Amorphous Carbon Bearing SO_3H, COOH, and OH Groups. J Am Chem Soc 2008; 130:12787–12793.

29. Zong M-H, Duan Z-Q, Lou W-Y, Smith TJ, Wu H. Preparation of a sugar catalyst and its use for highly efficient production of biodiesel. Green Chem 2007; 9:434–437.

30. Liu X-Y, Huang M, Ma H-L, Zhang Z, Gao J-M, Zhu Y-L, Han X, Guo X. Preparation of a Carbon-Based Solid Acid Catalyst by Sulfonating Activated Carbon in a Chemical Reduction Process. Molecules (Basel, Switzerland) 2010; 15:7188–96.

31. Wu M, Zeng W, He Q, Zhang J. Hydrothermal synthesis of SnO_2 nanocorals, nanofragments and nanograss and their formaldehyde gas-sensing properties. Materials Science in Semiconductor Processing 2013; 16:1495–1501.

32. Ahmed M, Rüsing M, Berth G, Lischka K, Pawlis A. CuO and Co_3O_4 Nanoparticles: Synthesis, Characterizations, and Raman Spectroscopy. Journal of Nanomaterials 2013; 2013:.

33. Xu JF, Ji W, Shen ZX, Li WS, Tang SH, Ye XR, Jia DZ, Xin XQ. Raman spectra of CuO nanocrystals. Journal of Raman Spectroscopy 1999; 30:413–415.

34. Liu Y, Miao X, Fang J, Zhang X, Chen S, Li W, Feng W, Chen Y, Wang W, Zhang Y. Layered-MnO_2 Nanosheet Grown on Nitrogen-Doped Graphene Template as a Composite Cathode for Flexible Solid-State Asymmetric Supercapacitor. ACS Appl Mater Interfaces 2016; 8:5251–5260.

Table 3. Shows the Average crystalline size, dislocation density and strain of the CuO and RACU samples

Sample Code	Average Crystalline Size (D) (nm)	Dislocation Density	Strain
CuO	61.09	2.67×10^{14}	0.00080
RACU1	49.70	4.04×10^{14}	0.00096
RACU2	42.20	5.61×10^{14}	0.00108
RACU3	54.50	3.36×10^{14}	0.00086

Table 4.The parameter of fitting line, BET constant and specific surface area

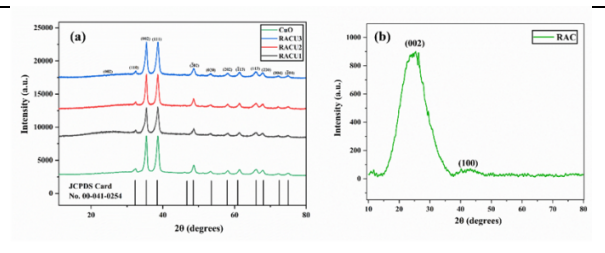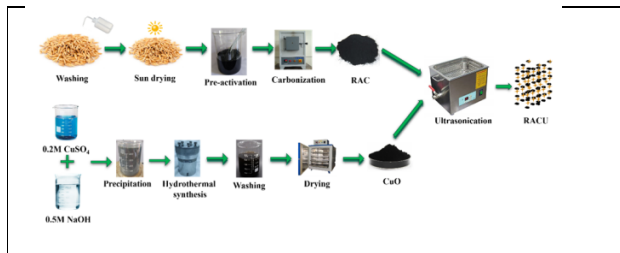| Sl. No	Sample	Relative pressure	Slope (s)	Intercept (i)	BET constant (C)	Specific surface area (m^2/g)	Total pore volume ($cm^3 g^{-1}$)	Mean pore diameter (nm)
1	RAC	0.0- 0.5	0.2029	0.00154	132.89	21.30	0.0564	10.605
2	RACU3	0.0- 0.5	0.2479	0.00254	98.732	21.58	0.1008	18.678

Jinitha *et al.,*

Figure 1 Shows the schematic illustration of synthesis of RACU

Figure 2 XRD of (a) CuO-decorated rice husk activated carbon(RAC/CuO) at three different ratios such as 1:1, 1:2 and 1:3 respectively and (b) Rice husk activated carbon (RAC)
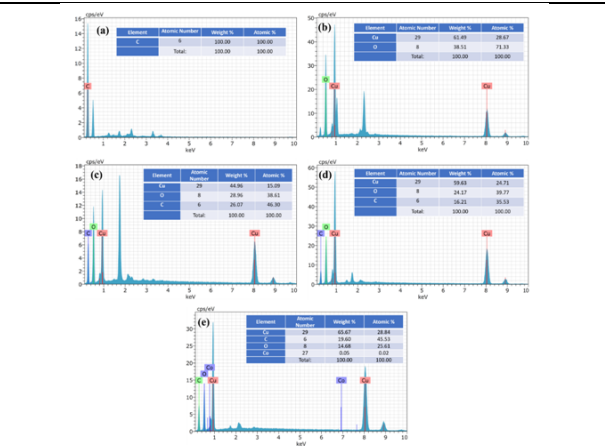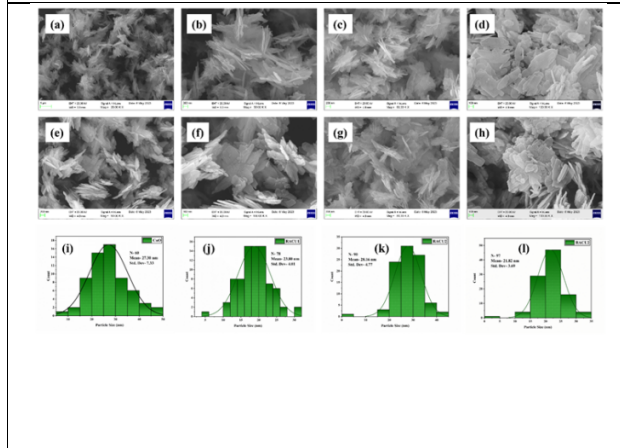

Figure 3 Shows the SEM image of (a, b)- CuO, (c, d)-RACU1, (e, f)-RACU2, (g, h)- RACU3 and the particle distribution curves of (i)- CuO, (j)- RACU1, (k)-RACU2 and (l)- RACU3 respectively

Figure 4 (a-e) Shows the EDX analysis of RAC, CuO, RACU1, RACU2, and RACU3 respectively
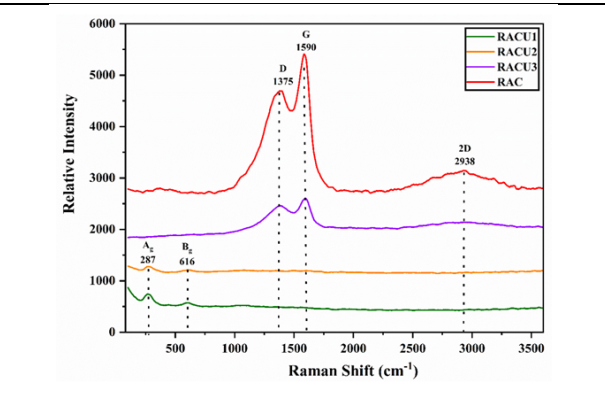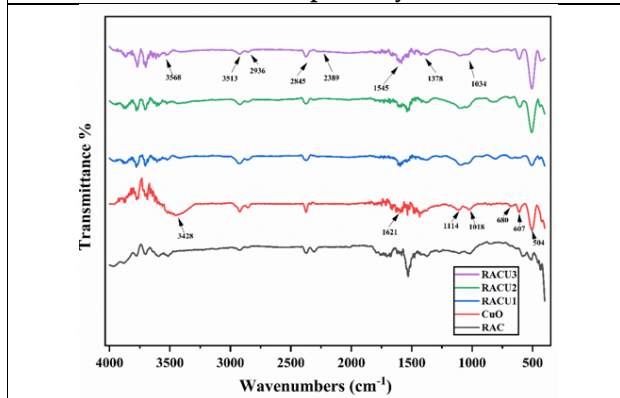
Figure 5 Shows the FTIR Spectra of the samples including RAC, CuO, RACU1, RACU2 and RACU3

Figure 6 Shows the Raman Spectra of RAC, RACU1, RACU2 and RACU3
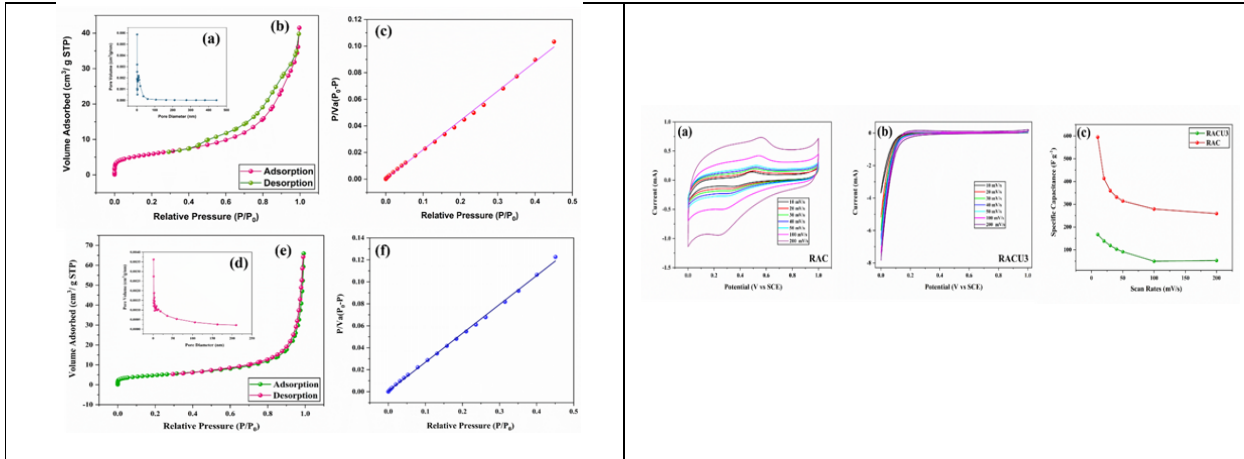
Jinitha *et al.,*

Figure 7 Shows (a) the pore size distribution of RAC, (b) the BET analysis of RAC, (c) the linear fitting plot of the RAC sample, (d) the pore size distribution of RACU3, (e) the BET analysis of RACU3, and (f) the linear fitting plot of RACU3 sample

Figure 8 (a)Shows the CV diagram of RAC (b) Shows the CV diagram of RACU3 sample and (c) shows the scan rate against specific capacitance plot of RAC and RACU3 sample
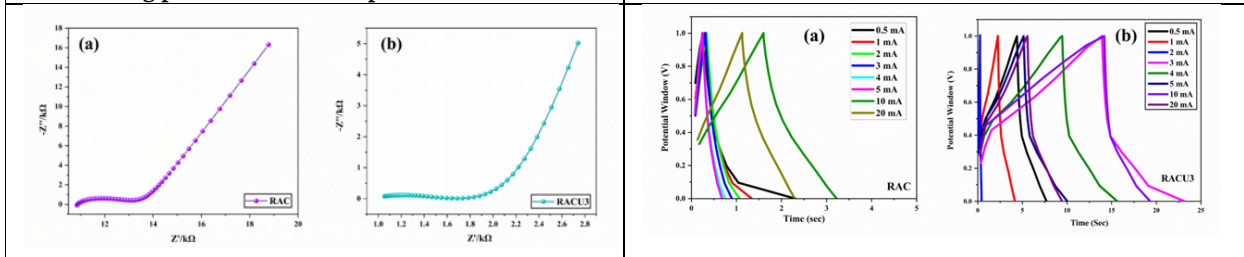

Figure 9 Shows the Electrochemical impedance spectra of (a) RAC and (b) RACU3
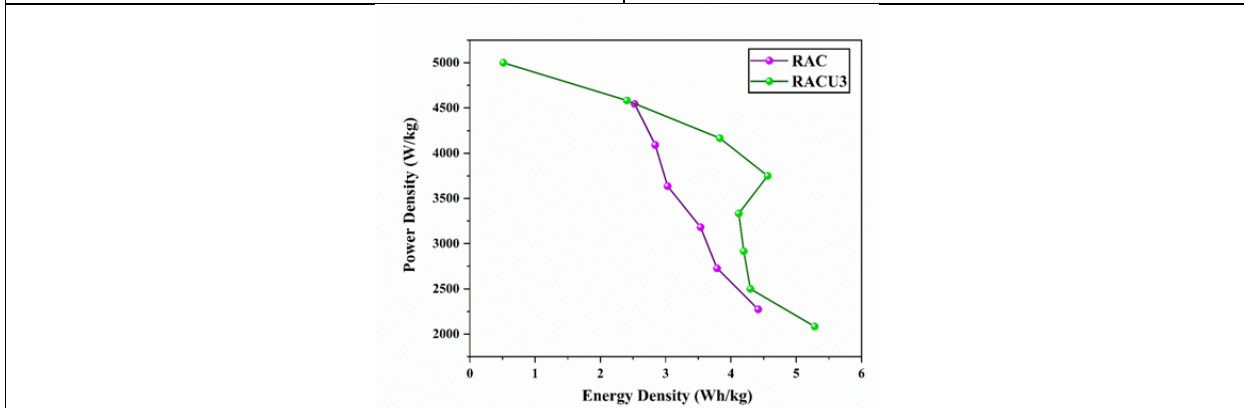
Figure 10 Shows the GCD plot of (a) RAC and (b) RACU3

Figure 11 Shows the Ragone plots of RAC and RACU3